Unsupervised-Learning-Based Feature-Level Fusion Method for Mura Defect Recognition

Shuang Mei, Hua Yang, *Member, IEEE*, and Zhouping Yin, *Member, IEEE*

***Abstract*—Mura defect recognition has long been a challenging task in displays, such as the liquid-crystal display (LCD), organic light-emitting diode display and polymer light-emitting diode display. In this paper, we propose an unsupervised-learning-based feature-level fusion approach for mura defect recognition. The approach is known as a joint-feature-representation-based defect recognition framework method. This method concentrates on obtaining effective and sufficient features for mura defects by fusing handcrafted and unsupervised-learned features in a complementary manner. To demonstrate the performance, several experiments are carried out to compare this method with some widely used feature extraction approaches. Experimental results show that the proposed method is more robust and accurate. They also indicate that it is compatible with different unsupervised-learning-based algorithms and handcrafted feature descriptors. Finally, the proposed method is implemented in the vision inspection equipment for recognizing mura defects in thin-film-transistor-LCD panels. It exhibits high robustness and improves the recognition performance by nearly 20% compared with the traditional handcrafted feature descriptors.**

***Index Terms*—Unsupervised learning, handcrafted feature, feature extraction, feature fusion, defect recognition.**

I. Introduction

IN RECENT years, the popularity of flat panel displays (FPDs), such as the LCD, OLED and PLED, has created fierce competition in the monitor industry. Thus, manufacturers have been devoting considerable efforts toward increasing production. Unfortunately, the complex manufacturing processes of these displays usually prevent the increase. Fig. 1 shows the display principle and structure of TFT-LCD. It is very complicated that many factors such as the nonuniform color of color filter substrate, the anisotropy of polarizer, the non-uniformly distributed liquid crystal material, the open or shorted scanning lines, the defective TFTs, the unevenness of TFT-array substrate, the foreign particles within liquid crystal, could cause diverse defects. Mura is a special type of these defects in the manufacturing processes. It refers to a local lightness variation on a surface without clear contours and causes an unpleasant sensation to the human vision [2]. The recognition of mura defects has long been a challenging task in visual inspection for FPDs.

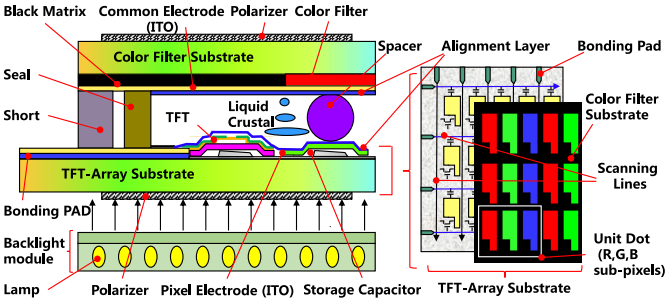

Fig. 1. Display principle and structure of TFT-LCD [1]. Mura defects are usually caused by defective color filter substrate, TFT-Array substrate, color filter, nonuniform liquid crystal and so on.

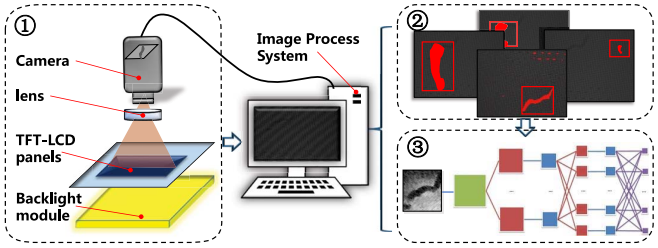

Fig. 2. Steps involved in inspection of mura defects by using the vision inspection equipment: ①: image acquisition, ②: defect detection, ③: defect recognition.

Mura defects are identified by experienced engineers or operators traditionally. However, this visual judgment method has drawbacks such as human fatigue and time wastage. In recent years, automatic visual inspection for mura defects has become possible with the development of machine vision technology. And it has gradually displaced the traditional manual inspection. The inspection of mura defects by visual inspection usually involves three steps, namely, image acquisition, defect detection and defect recognition, as shown in Fig. 2. In this paper, we mainly concentrate on the last step for mura defect recognition.

There are three main challenges in mura defect recognition task. First, mura defects generally appear as regions of low contrast and nonuniform brightness, typically larger than a single pixel in TFT-LCD panels [3]. Thus, it's difficult to recognize mura defects especially under nonuniform illumination conditions [2]. Second, mura defects appear as

Manuscript received July 3, 2016; revised November 18, 2016; accepted December 29, 2016. Date of publication January 5, 2017; date of current version February 1, 2017. This work was supported by the National Science Foundation of China under Grant 51327801, Grant 51475193, and the Major Project Foundation of Hubei Province under Grant 2016AAA009. *(Corresponding author: Hua Yang.)*

The authors are with the State Key Laboratory of Digital Manufacturing Equipment and Technology, Huazhong University of Science and Technology, Wuhan 430074, China (e-mail: huayang@hust.edu.cn).

Color versions of one or more of the figures in this paper are available online at http://ieeexplore.ieee.org.

Digital Object Identifier 10.1109/TSM.2017.2648856

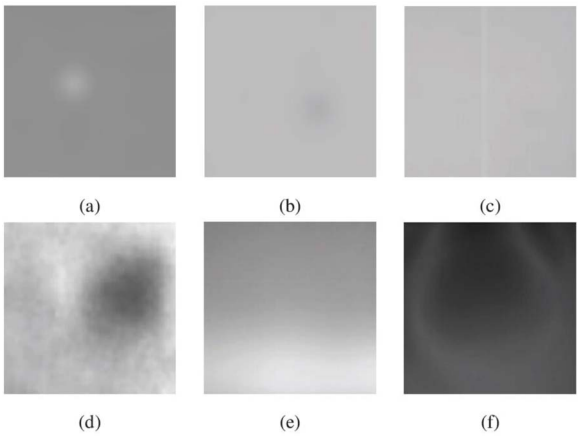

Fig. 3. Different types of mura defects. (a) The white spot, (b) black spot, (c) line, (d) region, (e) gravity, (f) and ring mura.

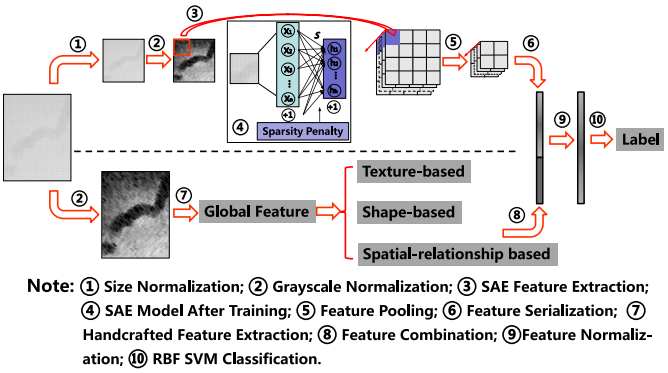

Fig. 4. The recognition process for a region mura defect using the proposed JFR-DRF method.

various irregular shapes, which contributes to the difficulties. Third, samples of mura defects are extremely scarce especially the gravity and ring mura, which may result in data imbalance. In this paper, we will mainly aim at recognition for the six common types of mura defects, as shown in Fig. 3.

There are many studies [4]–[8] which investigated in the detection phase of defects in TFT-LCD panels. While in the recognition phase, literatures are really rare. Even so, recognition of defects is still crucial and challenging. Using neural networks, Chen *et al*. [9] extracted features for defect classification and identification with a vision inspection equipment. They successfully recognized defects during the process of TFT-LCD photolithography manufacturing. However, this method is strict to the requirement of the samples. Further, Chen and Liu [10] adopted an adaptive resonance theory neural network and a self-organizing map to recognize similar defect spatial patterns on wafers with good performance. By comparing the similarity and then presenting a certain cluster, the defect type can be confirmed and then be used to aid in the diagnosis of failure causes. This method is not suitable for mura defect recognition because of the differences of mura defects themselves and the demand for online recognition. Tseng *et al*. [11] combined an artificial approach for defect feature extraction with a neural network and decision tree to classify defects in TFT-LCD color filters successfully. Chen *et al*. [12] utilized the artificial color features, shape features and statistical features for defect recognition in color filter manufacturing and achieved great effectiveness. Although using the artificial approaches exhibited relatively good performance in these applications, it is usually difficult for a human (even an experienced operator) to describe the inherent characteristics of objects. Thus, it may be insufficient for the recognition of mura defects.

As mentioned above, we can see that traditional handcrafted descriptors are able to perform well on many occasions, even though the occasions may have small number of samples. These descriptors have brought in human experience when designed, thus, they don't need any training process with large amount of data. However, such descriptors are limited in terms of extracting some high-level characteristics, such as the semantic information in images [13]. The unsupervised-learning-based feature extraction approaches have been proven to be effective in many fields [14]. They have much in common with the brain than supervised learning [15]. They also outperform supervised-learning-based methods on some occasions where labelling large amount of data is difficult or impossible. Thus, it is more suitable for mura defect recognition. However, both of them may suffer from information loss because of size-normalization of the training samples. In order to address the shortcomings of existing defect recognition methods, we propose a new scheme by fusing unsupervised-learned and handcrafted features to realize good performance for mura defect recognition and make it efficient to implement. The remainder of this paper is organized as follows. In Section II, we present the proposed JFR-DRF method for mura defect recognition in detail. Specifically, it elaborates strategies for training and testing the proposed method. Then, in Section III, the experimental results and analysis are provided . Finally, we conclude this paper in Section IV.

II. The JFR-DRF Method for Mura Defect Recognition

In this section, the proposed JFR-DRF method which attempts to make the handcrafted and the unsupervised-learned features complement with each other will be introduced. Then, strategies for training this model and recognizing mura defects will be described in detail.

A. Outline of the Proposed JFR-DRF Method

Mura defect recognition process with JFR-DRF is shown in Fig. 4. As can be seen, there are two streams, the unsupervised-learning-based stream and the handcrafted stream. The former uses the size-normalized image (after grayscale normalization), whereas the latter employs the original image (after grayscale normalization). This is required by the needs of their own models. Then, the features extracted by these two data streams will be merged into a single feature vector, which acts as the representation for the mura defect image. After subsequent processing, it will be classified using an one-against-all (OAA) SVM [16] classifier.

The flowchart of the proposed JFR-DRF method is shown in Fig. 5. There are three phases in it. The first two phases

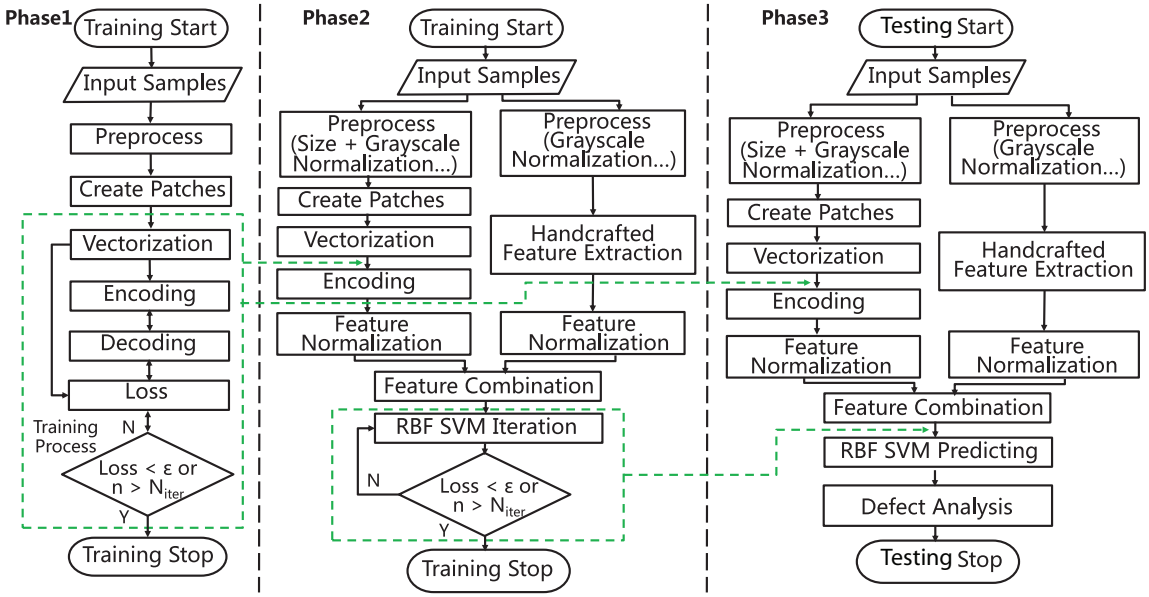

Fig. 5. Flowchart of the proposed JFR-DRF method. Phase1: Training phase for the unsupervised-learning-based feature extraction model. Phase2: Training phase for the OAA SVM classifier. Phase3: Recognition phase for a defect image. (The green dashed data streams refer to parameters sharing.)

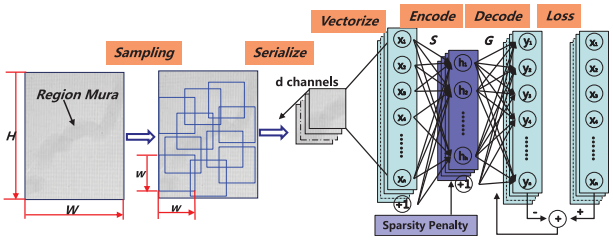

Fig. 6. Training processes using the proposed JFR-DRF method with the SAE algorithm.

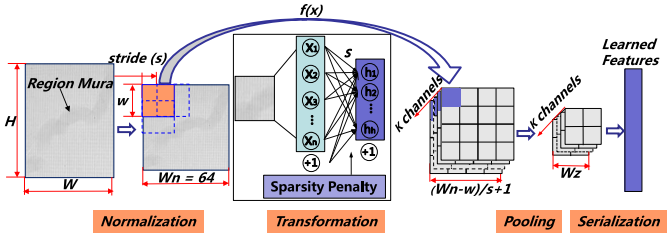

Fig. 7. Feature extraction using the proposed JFR-DRF method with the SAE algorithm.

refer to the training process and the third one refers to the recognition process. The unsupervised-learning-based feature-extraction steps (in Phase1) is compatible with different unsupervised learning algorithms (In the subsequent experiments, we will use sparse coding (SC) [17], sparse autoencoder (SAE) [18], K-means clustering (K-means) [19], restricted boltzmann machine (RBM) [20] and sparse filtering (SF) [21] for comparison). Here, the SAE algorithm will be taken as an example to elucidate the proposed JFR-DRF method. Processes for other algorithms are similar.

We use $f(\cdot)$ and $g(\cdot)$ as the feature extraction functions corresponding to the unsupervised-learning-based algorithms and the handcrafted methods. For a mura defect image I, the complete feature representation denoted by F_I can be expressed as

$$F_I = Vector\{f(I), \gamma \cdot g(I)\}, \gamma \in [0, 1], \quad (1)$$

where $Vector\{\cdot\}$ denotes the feature serialization process along the column direction, and γ denotes the weight between the unsupervised-learned and handcrafted features, which is a cross-validated parameter in the experiments.

It can be seen from Eq. (1) that the extraction of effective features is the key issue for mura defect recognition. The training phase for the unsupervised-learning-based feature-extraction process is shown in Fig. 6. It includes mainly the patch set preparation (patches are randomly sampled with size w×w in defect images) and training for the three layer neural networks. The corresponding feature extraction phase is shown in Fig. 7. It utilizes the trained model to transform the original image data to the feature domain. Handcrafted features for a mura defect image I can be expressed as $g(I)$. The feature extraction process is shown in Fig. 8. It is much succinct and time-saving than the $f(\cdot)$ process. These above-mentioned processes are steps for image representation. While for the identification procedure, we use an OAA SVM classifier. We will describe the proposed JFR-DRF method in detail as follows.

B. Training for the JFR-DRF Method

Training process for the proposed method includes training the unsupervised-learning-based model and the OAA SVM classifier. It is an offline process.

1) Training the Unsupervised-Learning-Based Model (SAE): As shown in Fig. 6, when training the unsupervised-learning-based feature extraction model, the patch set has been prepared. Then all patches in the patch set will be fed to the SAE model. Formally, the SAE model is an encode-decode process with the function $f : \Re^{N_I} \rightarrow \Re^{N_H} \rightarrow \Re^{N_O}$. N_I, N_H, and N_O represent the dimensions of the input layer,

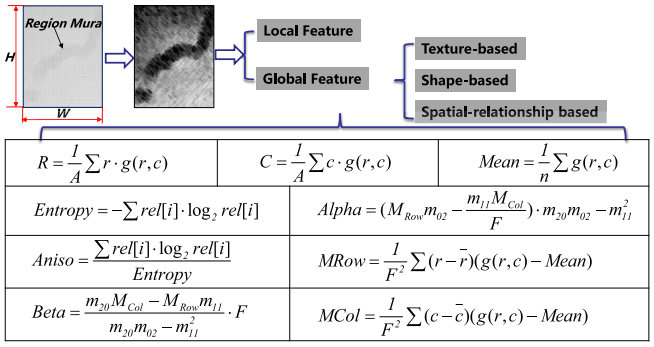

$R=\frac{1}{A}\sum r\cdot g(r,c)$	$C=\frac{1}{A}\sum c\cdot g(r,c)$	$Mean=\frac{1}{n}\sum g(r,c)$
$Entropy=-\sum rel[i]\cdot\log_2 rel[i]$	$Alpha=(M_{Row}m_{02}-\frac{m_{11}M_{Col}}{F})\cdot m_{20}m_{02}-m_{11}^2$	
$Aniso=\frac{\sum rel[i]\cdot\log_2 rel[i]}{Entropy}$	$MRow=\frac{1}{F^2}\sum(r-\bar{r})(g(r,c)-Mean)$	
$Beta=\frac{m_{20}M_{Col}-M_{Row}m_{11}}{m_{20}m_{02}-m_{11}^2}\cdot F$	$MCol=\frac{1}{F^2}\sum(c-\bar{c})(g(r,c)-Mean)$	

Fig. 8. Feature extraction using the proposed JFR-DRF method with hand-crafted descriptors. Here, R, C denote the gravity center of the image; *Mean* denotes the mean grayscale value; *Entropy*, *Aniso* denote the entropy and anisotropy coefficients based on the grayscale histogram; *Beta*, *Alpha* denote the grayscale value moments; and M_{Row}, M_{Col} denote the mixed moments along row and column direction. For further details, please refer to [24].

hidden layer, and output layer. In matrix notation, the feature transformation process can be expressed as

$$h = S(x \cdot W + b),$$
$$y = G\big(h \cdot W' + b'\big), \tag{2}$$

where W and W' are the convolution kernel, b and b' are the bias-based coefficients, and h, y are the outputs of the encoding and decoding phases. Further, S and G represent the activation function. Here, we use the *sigmoid* function [22]. The loss function of this model can be measured as

$$L = \min_{W,W',b,b'} \frac{1}{m}\sum_{i=1}^{m}\left\|y_I^{(i)} - x_I^{(i)}\right\|^2 + \lambda \sum_{w\in W,W'} \|w\|_F^2 + \beta\sum_{i=1}^{N_H} KL\big(\rho\|\hat{\rho}_i\big), \tag{3}$$

where

$$KL\big(\rho\|\hat{\rho}_i\big) = \rho log\frac{\rho}{\hat{\rho}_i} + (1-\rho)log\frac{1-\rho}{1-\hat{\rho}_i}. \tag{4}$$

The λ and β are non-negative constants which can be determined using cross-validation, the *KL* divergence [23] is used to prevent degradation in the model. $\hat{\rho}_i$ refers to the average activation response of the i-th neuron in the hidden layer, ρ is a hyper-parameter. The representation $h_I^{(i)}$ with smallest reconstruction error is considered as the features of the original patch $x_I^{(i)}$. After training, the SAE model can be adopted to encode patches to the feature domain.

Detailed training procedures of the proposed JFR-DRF method with the SAE algorithm are summarized in Table I.

2) Training Process for the OAA SVM Classifier: Training process for the OAA SVM classifier includes data preparation and SVM training, as shown in Phase2 (Fig. 5). The process for data preparation here is much similar to that for recognizing a defect image (Phase3 in Fig. 5), so it will not be repeated here. While for the SVM training (also SVM predicting), we use the off-the-shelf SVM lib [25].

C. Recognition With the JFR-DRF Method

Mura defect recognition with the proposed JFR-DRF method is an online process. Before this process, training for

TABLE I
TRAINING PHASE OF THE UNSUPERVISED-LEARNING-BASED FEATURE-EXTRACTION MODEL

Declaration : Original mura defect image dataset ζ_0 (mura defect images may have different sizes), number of total images in ζ_0 is N_0, image size after size-normalization is $W_n \times W_n$, dataset after normalization is ζ_n, number of patches extracted from each defect image is N_T, and the size of each patch is w×w. The patch set is ζ, the i-th patch is $x^{(i)}$, number of patches in ζ is N_p (N_p is an integer multiple of N_T). Number of epoch iterations is N_{iter}. Iterative termination error is ε. Number of neurons in the input layer, hidden layer and output layer are N_I,N_H and N_O (N_I=N_O in SAE). The learning rate is lr.

Procedure

1. Normalize each image in ζ_0 to uniform size $W_n \times W_n$, $\zeta_0 \rightarrow \zeta_n$;
2. Normalize brightness and contrast for all images using the whitening process [26] in ζ_n;
3. Randomly select N_p/N_T images in step2;
4. Randomly select N_T patches with size w×w for each image in step3;
5. Vectorize all the patches in step4 and generate the sequence ζ, $\zeta = \{x^{(1)},x^{(2)},\cdots,x^{(N_p)}\}$;
6. Initialize parameter, $\delta = 4\sqrt{6/(N_I+N_H)}$, $W = \{w_{i,j}\}$, $w_{i,j} \sim U(-\delta,\delta)$; $W' = \{w'_{i,j}\}$, $w'_{i,j} \sim U(-\delta,\delta)$; $b = 0, b' = 0$; $\varepsilon = 0.05$, $N_{iter} = 100$, $lr = 0.1$, $L = \inf$, $n = 0$;
7. **While** $(L > \varepsilon \;\&\; n < N_{iter})$ **do**
   Calculate L with Eq. (3), calculate the partial derivatives;
   $\triangle W \leftarrow \partial L/(\partial W)$, $\triangle b \leftarrow \partial L/(\partial b)$;
   $\triangle W' \leftarrow \partial L/(\partial W')$, $\triangle b' \leftarrow \partial L/(\partial b')$;
   $W \leftarrow W - lr\cdot \triangle W$, $b \leftarrow b - lr\cdot \triangle b$;
   $W' \leftarrow W' - lr\cdot \triangle W'$, $b' \leftarrow b' - lr\cdot \triangle b'$;
   $n \leftarrow n+1$;
   end While
8. Save the learned model.

the unsupervised learning based model and the SVM classifier are both finished. The recognition phase is shown in Phase3 (Fig. 5). It includes feature extraction, feature fusion and classification processes, which will be elaborated as follows. Before these process, the image preprocessing will be conducted first.

1) Image Preprocessing: The whitening process [26] are conducted for each defect image before training and testing processes to remove or lower correlations among samples.

2) Feature Extraction by the Unsupervised Learning Algorithm: Feature extraction by the unsupervised-learning-based model must be conducted under the premise that this model has been well trained. With the trained model, patches with size w×w can be encoded by the feature extractor $S : \Re^{N_I} \rightarrow \Re^{N_H}$, as shown in Fig. 7. The function $S(\cdot)$ refers to Eq. (2). For a mura defect image I with size $W \times H$, it will be normalized to the uniform size $W_n \times W_n$ first. Then patches will be extracted from this normalized image and transferred to the feature domain; for the i-th patch, $x_I^{(i)} \rightarrow h_I^{(i)}$, where $h_I^{(i)}$ acts as the learned feature. Finally, we can get a matrix of size $[(W_n-\mathrm{w})/s+1] \times [(W_n-\mathrm{w})/s+1] \times N_H$ by applying the feature extractor S to all of the patches, w is the size of the convolutional kernel, s is the slide interval. The proposed matrix is represented as the feature representation matrix of the original defect image. Typically, this matrix has a large dimension. For computational efficiency, a mean-pooling process is applied. The feature representation matrix will be pooled to a new shape with size $2 \times 2 \times N_H$, as shown in Fig. 7. Thus, the unsupervised-learned feature can be expressed as

$$f(I) = p\Big(h_I^{(1)}, h_I^{(2)}, \ldots, h_I^{(N_p)}\Big) \tag{5}$$

where $p(\cdot)$ denotes the mean-pooling process.

TABLE II
DISTRIBUTION OF THE SIX CATEGORIES OF MURA DEFECTS

Type	Black spot mura	White spot mura	Gravity mura
No. of samples	3127	3291	1888
Type	Line mura	Region mura	Ring mura
No. of samples	1876	2387	1922

TABLE III
RECOGNITION PHASE OF JFR-DRF BY USING THE SAE ALGORITHM

Declaration: The candidate mura defect image is $\tilde{\mathrm{I}}$, image after size-normalization is I, the i-th patch of image I is $x_I^{(i)}$, features extracted by the unsupervised learning based method and handcrafted descriptors are F_L and F_H, feature representation for image I is F_I.

Procedure

Process1 Feature extraction by unsupervised learning based method

1. Normalize brightness and contrast for image $\tilde{\mathrm{I}}$ and get the normalized image I;
2. Normalize image I in step1 with bilinear interpolation to uniform size $W_n \times W_n$;
3. Extract patches with size w×w for image in step2 and get the patch set $\zeta_I = \{x_I^{(1)}, x_I^{(2)}, \cdots x_I^{(N)}\}$, $N = [(W_n - \mathrm{w})/s + 1] \times [(W_n - \mathrm{w})/s + 1]$;
4. For each $x_I^{(i)}$ in ζ_I , encode it with Eq. 2 and get the feature $h_I^{(i)}$;
5. Gain the feature representation matrix $H_I = \{h_I^{(1)}, h_I^{(2)}, \cdots h_I^{(N)}\}$;
6. Pooling H_I in step5 to size $2 \times 2 \times N_H$, as shown in Fig. 7;
7. Vectorize matrix in step6 and get the unsupervised-learned feature $F_L^{'}$.
8. Normalize $F_L^{'}$ in step 7 from interval (min, max) to $(0, 1)$ and get the normalized feature F_L.

Process2 Feature extraction by artificial method

9. Compute the handcrafted feature of image $\tilde{\mathrm{I}}$, as shown in Fig. 8, then get the handcrafted feature $F_H^{'}$;
10. Normalize $F_H^{'}$ in step9 from interval (min, max) to $(0, 1)$ and get the normalized feature F_H.

Process3 Feature fusion and classification

11. Gain the final feature F_I with Eq. 1;
12. Classify the defect image $\tilde{\mathrm{I}}$ with the trained OAA SVM classifier.

3) Feature Extraction by the Handcrafted Descriptors: As stated, handcrafted descriptors have been brought in human experience when designed, and they don't need any training process. Here, we use the gravity positions, gray value histogram, entropy, anisotropy and moments to describe the defects, as shown in Fig. 8. For detailed calculations of these attributes, we can refer to [24].

4) Feature Fusion and Classification Process: Features extracted by the unsupervised-learning-based model and the handcrafted descriptors are concatenated to form the representations of defect images. Then, normalization will be adopted to map features in each component from interval (*min*, *max*) to (0, 1) with linear interpolation; thus, features that are not in the same domain can be merged. Defect classification is carried out using the off-the-shelf SVM lib [25] with the radial basis function (RBF) kernel (Parameter $t = 2$).

Detailed procedures for mura defect recognition with the proposed JFR-DRF method are introduced in Table III.

D. Computational Complexity Analysis

The computational complexity analysis is necessary for online mura defect recognition. It affects the production efficiency directly. The training phases for both the unsupervised learning model and the OAA SVM classifier are offline processes, which are conducted in advance. They don't affect the time taken by the recognition procedure. Here, we will analyze the computational complexity which mainly aims to the recognition procedure for a mura defect.

The so called computational complexity mainly refers to the analysis of algorithms [27], which depends on the architecture of the models. It is affected by the most nested-loop parts of the models. In the procedure described in Table III, the most time-consuming and nested-loop steps are step3 (step to gain the patch set) and step4 (step to encode the patch set and obtain features). Complexity for step3 roughly corresponds to the circulatory serialization to patches. Using T_c donates the computational complexity, for step3, $T_c(step3) = (W_n - \mathrm{w}+1)^2 \cdot \mathrm{w}^2 = O(W_n^2)$ (W_n is much larger than w). The $(W_n - \mathrm{w}+1)^2$ and w^2 refer to numbers of the iterations and the basic operations in serialization for each patch. Step4 with the SAE algorithm can be viewed as a multilayer perception type artificial neural network with one hidden layer. According to [28], the computational complexity for step4 can be estimated as $T_c(step4) = N_H \cdot (W_n - \mathrm{w}+1)^2 \cdot \mathrm{w}^2 = O(W_n^2)$. Taking the results in step3 and step4 into consideration, the computational complexity for recognizing a defect image is $O(W_n^2)$.

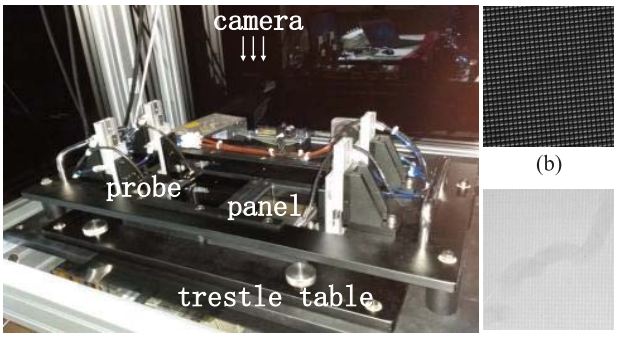

Fig. 9. The vision inspection test bench and defect image used in the experiments. (a) The test bentch with two TFT-LCD panels inspected. (b) The original defect image with an region mura. (c) Defect image with texture removed.

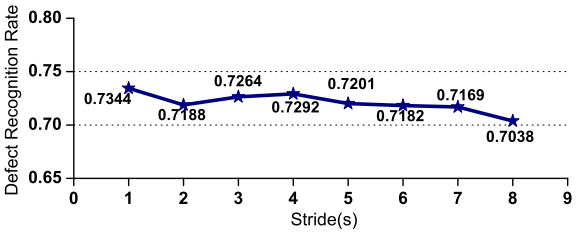

Fig. 10. Average effect of stride *s* using different unsupervised-learning algorithms on mura defect testing set with stride *s* varies from 1 to 8.

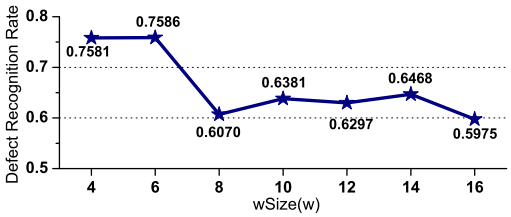

Fig. 11. Average effect of receptive field size *w* using different unsupervised-learning algorithms on mura defect testing set with *w* varies from 4 to 16 with step 2.

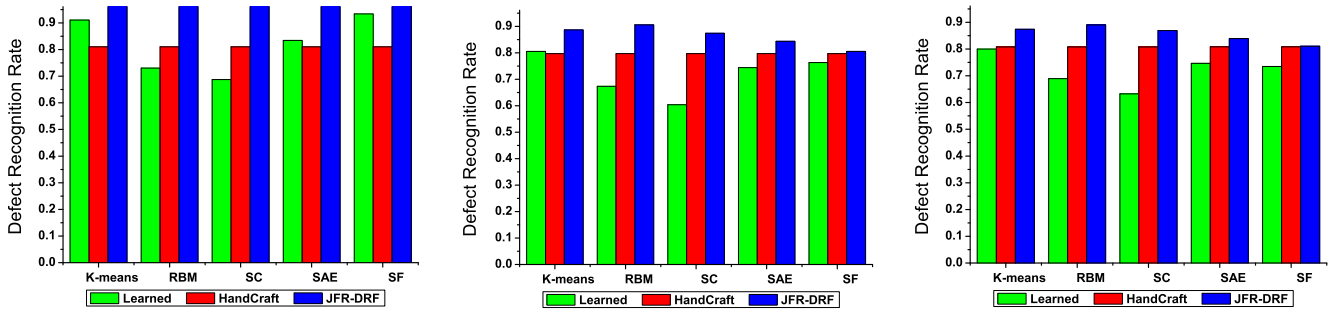

Fig. 12. Overall recognition performance comparison using only unsupervised-learned features, only handcrafted features, and features gained by the proposed JFR-DRF method: (a) performance on the mura defect training set, (b) validation set, (c) and testing set.

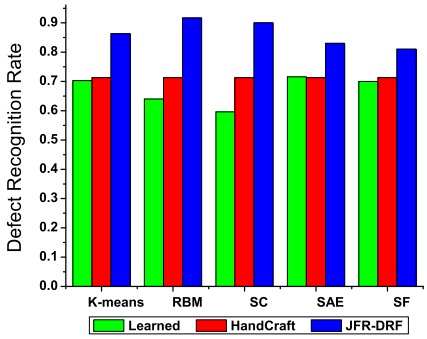

Fig. 13. Recognition performance on the confused dataset using only unsupervised-learned features, only handcrafted features, and features gained by the proposed JFR-DRF method.

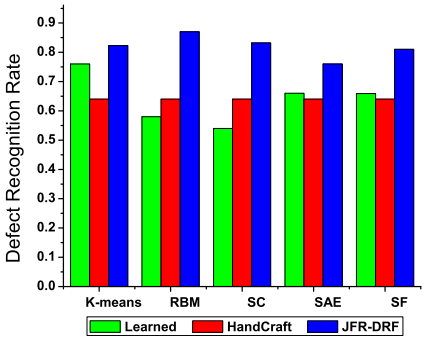

Fig. 14. Recognition performance on the blurry dataset using only unsupervised-learned features, only handcrafted features, and features gained by the proposed JFR-DRF method.

The handcrafted feature-extraction process can be conducted in parallel with the learning-based process and is relatively time-saving, so it is negligible.

Performance for the proposed JFR-DRF method will be discussed in Section III.

III. Experimental Results and Discussion

A. Experimental Preparation

1) Experimental Environment and Dataset: By using the vision inspection equipment, defective images for TFT-LCD panels were collected and stored for subsequent analysis. Fig. 9(a) shows the vision inspection test bench used in our experiments for mura defect inspection. Two panels are detected simultaneously. Fig. 9(b) shows an defective image captured by an industrial camera. The image is filled with periodic textures caused by the RGB pixels in TFT-LCD panels. Fig. 9(c) exhibits the image with texture removed and it will be used for recognition.

The distribution of mura defects is presented in Table II. 14491 grayscale mura defect images are collected. Some types of the defects, such as the ring mura defects, are extremely rare in TFT-LCD panels. Therefore, parts of the images in the defect image dataset were obtained using data augmentation [29]. This ensures the relative balance in each category of mura defects. For the unsupervised-learning-based model, we normalized all of the defect images to a uniform size 64×64. Further, 10000 defect images were used for training, 2000 for validation and 2491 for testing in later experiments.

2) Model Parameter Analysis: Many factors may affect the final identification of mura defects in the JFR-DRF method, such as the types and parameters of the unsupervised-learning-based algorithms. The impact of different unsupervised-learning-based algorithms will be analyzed in Section III-B. Here, we will mainly analyze the parameter s, which represents the slide interval of the two adjacent patches, and w, which represents the size of the local receptive field [30] (also size of the convolutional kernel), as shown in Fig. 7.

Fig. 10 shows the recognition performance on the mura defect testing set with stride s varies from 1 to 8. It's an average result using the SAE, K-means, SC, SF, and RBM algorithms. As can be seen, the recognition performance shows a relatively slow downward trend when stride s is increased. This is consistent with the results presented in [18]. Generally, with smaller s, it is possible to get better results. Thus, the parameter stride s with value 1 will be used in the following experiments.

The receptive field is a concept derived from neuroscience. In the experiments, we varied the receptive field size w from 4 to 16 with step 2. A very large or very small receptive field size may increase the computational complexity sharply. As shown in Fig. 11, we can get the relatively best recognition performance when $w = 6$. This is also consistent with the results presented in [18], which cross-validated the parameter w on CIFAR-10 dataset and got the best result at the 6 pixels receptive field.

The dimension of the feature space domain was verified in our experiments with the following sizes: 100, 200, 400,

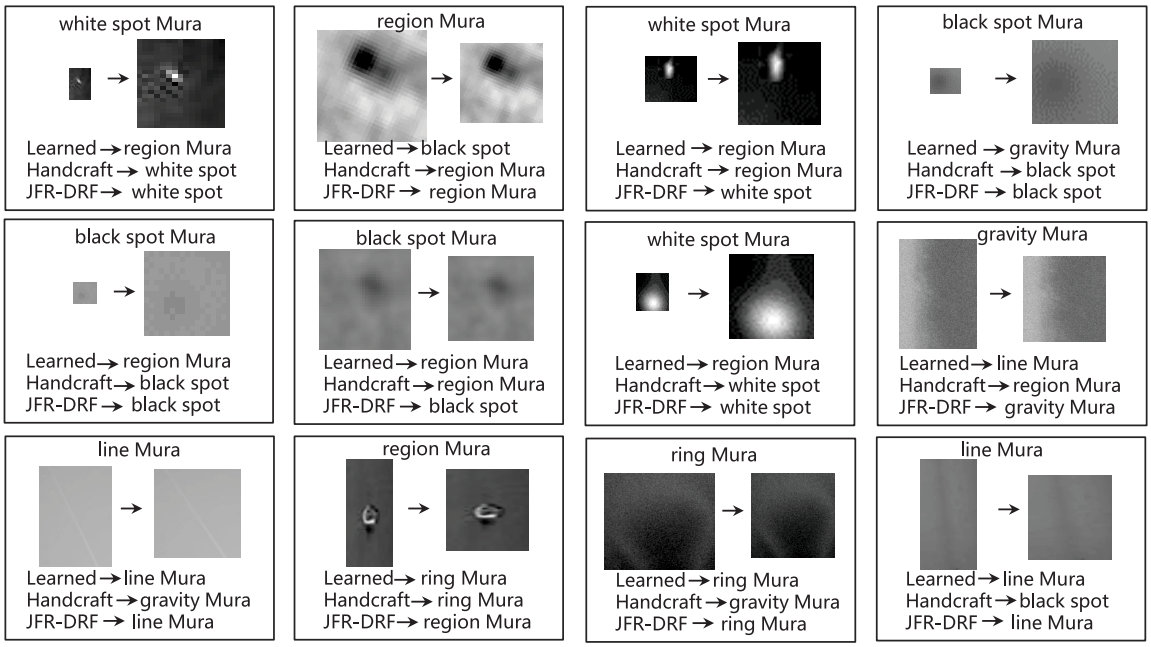

Fig. 15. Visualization of some mura defect samples that were incorrectly identified by the unsupervised-learning-based methods and the handcrafted descriptors while correctly identified by the proposed JFR-DRF method.

800 and 1200. We found that the accuracy of mura defect recognition improved when the dimension of the feature space domain increased. In order to achieve a tradeoff between the recognition rate and the computational complexity, we set the dimension to 200, the size of the local receptive field w to 6, and the sliding interval *s* to 1 in later experiments.

B. Experimental Results

1) Comparison of Experimental Results: Features extracted by the handcrafted descriptors are fused to the unsupervised-learned features in the proposed JFR-DRF method, the mean recognition accuracy is used as the evaluation criterion. Fig. 12(a-c) shows the recognition rate using different methods on the mura defect training set, validation set, and testing set. As can be seen in Fig. 12(a), mura defect recognition rate on the training set can be significantly improved by the JFR-DRF method. In particular, by using SC algorithm, the JFR-DRF outperforms methods which utilize only unsupervised-learned features by nearly 30% and methods which utilized only handcrafted features by nearly 20%. Fig. 12(b) and Fig. 12(c) show similar performance. It can be concluded that using the JFR-DRF method can improve mura defect recognition performance to some extent regardless of the selected unsupervised-learning-based methods, and it usually obtains better feature representations than single feature-extraction methods.

2) Analysis of the Experimental Results: Here, we will explore the reason why recognition performance can be improved by using the JFR-DRF method with some extra experiments.

We re-collected two datasets with different categories of mura defects. One contains 300 sample images and mainly includes small-spot and large-region mura defects. These images show large deformations when size-normalization is applied. We named this dataset the confused dataset. The another dataset contains 180 sample images and includes samples with relatively blurry background. It is mainly composed of the gravity and ring mura defects. We named it the blurry dataset.

Recognition performance on the confused dataset and the blurry dataset is shown in Fig. 13, Fig. 14. We can see that the methods using only unsupervised-learned features perform poorest on the former while the methods using only handcrafted features perform poorest on the later dataset. The proposed JFR-DRF method is the best. Results on these two extra experiments have verified some previous statements. That is, the shapes, structures, and spatial relationships are changed when applying size-normalization to mura defect images by using the unsupervised learning based methods. Therefore the categories of mura defects tend to be misjudged. While the handcrafted descriptors take the raw defect images as inputs and retain information that maybe lost in the unsupervised-learning-based methods. It is true especially for small-spot and large-region mura defects. While on the blurry dataset, it is relatively difficult to describe the inner properties, such as the structural information and semantic information using traditional handcrafted descriptors. This is true especially for the gravity and ring mura defects. The proposed JFR-DRF method utilizes both features extracted by the unsupervised-learning-based method and the handcrafted descriptors, thus it trends to perform better. In order to further verify this conclusion, we show the p-Value rate on these two datasets in Table IV. It also indicates that the JFR-DRF method is more robust and sufficient.

Further, we visualize performance of the JFR-DRF method on the confused and blurry datasets, as shown in Fig. 15. Some mura defect images which are successfully recognized

TABLE IV
THE MEAN P-VALUE PERFORMANCE USING DIFFERENT METHODS, ①: THE UNSUPERVISED-LEARNING-BASED METHODS, ②: THE HANDCRAFTED METHODS, ③: THE PROPOSED JFR-DRF METHOD

Model	Confused Dataset			Blurry Dataset		
	①	②	③	①	②	③
K-means	0.30	0.28	**0.14**	0.24	0.36	**0.18**
RBM	0.36	0.28	**0.08**	0.42	0.36	**0.13**
SC	0.40	0.28	**0.10**	0.46	0.36	**0.17**
SAE	0.28	0.28	**0.17**	0.34	0.36	**0.24**
SF	0.30	0.28	**0.19**	0.34	0.36	**0.19**

by using JFR-DRF are shown. While they are failed to be identified by using the unsupervised learning based models and the handcrafted descriptors.

IV. CONCLUSION

The proposed model JFR-DRF utilized both unsupervised-learned and handcrafted features to generate a more discriminative representation for mura defect recognition and achieved good performance. Experiments show that features learned by JFR-DRF are more robust and stable when compared with other single-modality descriptors. They also noted that the JFR-DRF method is compatible with different representations no matter they are learned or handcrafted. The inspiration of designing JFR-DRF to gain an intact feature presentation by combining features from multiple modalities is crucial and can be easily applied in many other applications. However, fused feature representations may also have the risk of being affected by poor representations from modalities which are not appropriate for the tasks. Removing poor representations and enhancing effective ones is subsequent subject for further research.

REFERENCES

[1] *TFT-LCD Process—What Is TFT-LCD*, AU Optronics Corporat., Hsinchu, Taiwan, 2016. [Online]. Available: http://auo.com/?sn=189&lang=en-US

[2] S.-K. S. Fan and Y.-C. Chuang, "Automatic detection of Mura defect in TFT-LCD based on regression diagnostics," *Pattern Recognit. Lett.*, vol. 31, no. 15, pp. 2397–2404, 2010.

[3] W.-K. Pratt, S.-S. Sawkar, and K. O'Reilly, "Automatic blemish detection in liquid crystal flat panel displays," in *Proc. Symp. Electron. Imag. Sci. Technol.*, San Jose, CA, USA, 1998, pp. 2–13.

[4] J. Y. Lee and S. I. Yoo, "Automatic detection of region-Mura defect in TFT-LCD," *IEICE Trans. Inf. Syst.*, vol. E87-D, no. 10, pp. 2371–2378, Oct. 2004.

[5] L.-C. Chen and C.-C. Kuo, "Automatic TFT-LCD Mura defect inspection using discrete cosine transform-based background filtering and 'just noticeable difference' quantification strategies," *Meas. Sci. Technol.*, vol. 19, no. 1, 2007, Art. no. 015507.

[6] J. H. Oh *et al.*, "Line defect detection in TFT-LCD using directional filter bank and adaptive multilevel thresholding," *Key Eng. Mater.*, vols. 270–273, pp. 233–238, Aug. 2004.

[7] Y.-C. Song, D.-H. Choi, and K.-H. Park, "Morphological blob-Mura defect detection method for TFT-LCD panel inspection," in *Proc. Int. Conf. Knowl. Based Intell. Inf. Eng. Syst.*, vol. 270. Wellington, New Zealand, 2004, pp. 862–868.

[8] S.-H. Chen and D.-B. Perng, "Directional textures auto-inspection using principal component analysis," *Int. J. Adv. Manuf. Technol.*, vol. 55, nos. 9–12, pp. 1099–1110, 2011.

[9] L.-F. Chen, C.-T. Su, and M.-H. Chen, "A neural-network approach for defect recognition in TFT-LCD photolithography process," *IEEE Trans. Electron. Packag. Manuf.*, vol. 32, no. 1, pp. 1–8, Feb. 2009.

[10] F.-L. Chen and S.-F. Liu, "A neural-network approach to recognize defect spatial pattern in semiconductor fabrication," *IEEE Trans. Semicond. Manuf.*, vol. 13, no. 3, pp. 366–373, Sep. 2000.

[11] D.-C. Tseng, I.-L. Chung, P.-L. Tsai, and C.-M. Chou, "Defect classification for LCD color filters using neural-network decision tree classifier," *Int. J. Innov. Comput. Inf. Control*, vol. 7, no. 7, pp. 3695–3707, 2011.

[12] Y.-J. Chen, T.-H. Lin, K.-H. Chang, and C.-F. Chien, "Feature extraction for defect classification and yield enhancement in color filter and microlens manufacturing: An empirical study," *J. Ind. Prod. Eng.*, vol. 30, no. 8, pp. 510–517, 2013.

[13] X. S. Zhou and T. S. Huang, "CBIR: From low-level features to high-level semantics," in *Proc. Int. Soc. Opt. Photon. Electron. Imag.*, San Jose, CA, USA, 2000, pp. 426–431.

[14] A. Coates, A. Karpathy, and A. Y. Ng, "Emergence of object-selective features in unsupervised feature learning," in *Proc. Adv. Neural Inf. Process. Syst.*, pp. 2681–2689, 2012.

[15] P. Dayan, "Unsupervised learning," in *The MIT Encyclopedia of the Cognitive Sciences*. Cambridge, MA, USA: MIT Press, 1999.

[16] J. Weston and C. Watkins, "Multi-class support vector machines," Dept. Comput. Sci., Royal Holloway Univ. London, Egham, U.K., Tech. Rep. CSD-TR-98-04, 1998.

[17] B. A. Olshausen and D. J. Field, "Sparse coding with an overcomplete basis set: A strategy employed by V1?" *Vis. Res.*, vol. 37, no. 23, pp. 3311–3325, 1997.

[18] A. Coates, A. Y. Ng, and H. Lee, "An analysis of single-layer networks in unsupervised feature learning," in *Proc. Int. Conf. Artif. Intell. Stat.*, Fort Lauderdale, FL, USA, 2011, pp. 215–223.

[19] C. Ding and X. He, "K-means clustering via principal component analysis," in *Proc. 21st Int. Conf. Mach. Learn.*, Banff, AB, Canada, 2004, p. 29.

[20] B. M. Marlin, K. Swersky, B. Chen, and N. D. Freitas, "Inductive principles for restricted Boltzmann machine learning," in *Proc. Int. Conf. Artif. Intell. Stat.*, 2010, pp. 509–516.

[21] J. Ngiam, Z. Chen, S. A. Bhaskar, P. W. Koh, and A. Y. Ng, "Sparse filtering," in *Proc. Adv. Neural Inf. Process. Syst.*, Granada, Spain, 2011, pp. 1125–1133.

[22] P. Sibi, S. A. Jones, and P. Siddarth, "Analysis of different activation functions using back propagation neural networks," *J. Theor. Appl. Inf. Technol.*, vol. 47, no. 3, pp. 1264–1268, 2013.

[23] C. M. Bishop, "Variational principal components," in *Proc. 9th Int. Conf. Artif. Neural Netw.*, vol. 1. Edinburgh, U.K., 1999, pp. 509–514.

[24] H. Version, *HALCON/HDevelop Reference Manual 11.0.1*, MVTec Softw. GmbH, Munich, Germany, 2012.

[25] R. Fan, P. Chen, and C. Lin, "Working set selection using second order information for training support vector machines," *J. Mach. Learn. Res.*, vol. 6, no. 12, pp. 1889–1918, 2005.

[26] A. Kessy, A. Lewin, and K. Strimmer, "Optimal whitening and decorrelation," *arXiv preprint arXiv:1512.00809*, 2015.

[27] S. Arora and B. Barak, *Computational Complexity: A Modern Approach*. Cambridge, U.K.: Cambridge Univ. Press, 2009.

[28] G. Serpen and Z. Gao, "Complexity analysis of multilayer perceptron neural network embedded into a wireless sensor network," *Procedia Comput. Sci.*, vol. 36, pp. 192–197, Nov. 2014.

[29] X. Cui, V. Goel, and B. Kingsbury, "Data augmentation for deep neural network acoustic modeling," *IEEE/ACM Trans. Audio, Speech, Language Process.*, vol. 23, no. 9, pp. 1469–1477, Sep. 2015.

[30] H. G. Krapp and R. Hengstenberg, "A fast stimulus procedure to determine local receptive field properties of motion-sensitive visual interneurons," *Vis. Res.*, vol. 37, no. 2, pp. 225–234, 1997.

Shuang Mei received the B.S. degree in mechanical electronic and information engineering from the China University of Geoscience, Wuhan, China, in 2012. He is currently pursuing the Ph.D. degree with the State Key Laboratory of Digital Manufacturing Equipment and Technology, Huazhong University of Science and Technology, Wuhan.

His current research interests include image defect detection, pattern recognition, and electronic equipment manufacturing.

Hua Yang received the B.S. and M.S. degrees from the Huazhong University of Science and Technology, Wuhan, China, in 2006 and 2008, respectively, and the Ph.D. degree from Hiroshima University, Japan, in 2011. He was with Hiroshima University, as a Research Associate, from 2011 to 2012, and an Assistant Professor, in 2012, for seven months. He is currently an Associate Professor with the School of Mechanical Science and Engineering, Huazhong University of Science and Technology.

His current research interests include high-speed vision and its applications (object recognition, detection and tracking, particle image velocity, and dynamics-based vision inspection).

Zhouping Yin received the B.S., M.S., and Ph.D. degrees from the Huazhong University of Science and Technology, Wuhan, China, in 1994, 1996, and 2000, respectively, all in mechanical engineering. He is a Professor with the School of Mechanical Science and Engineering. Since 2005, he has been the Vice Head of the State Key Laboratory of Digital Manufacturing Equipment and Technology. He was a Cheung Kong Chair Professor in 2009. He is or has been a Principal Investigator for projects sponsored by General Program and Major Program of the National Science Foundation of China, the National Basic Research Project of China, and others. He has published two monographs, three chapters in English books, and over 30 papers in international journals such as the IEEE TRANSACTIONS, *ASME Transaction*, and *Computer-Aided Design*. He is leading a research group and conducting research in electronic manufacturing equipment and technology, including flexible electronics and electronic packaging. He was a recipient of the China National Funds for Distinguished Young Scientists in 2006.